INSTITUTE OF PHYSICS PUBLISHING JOURNAL OF OPTICS A: PURE AND APPLIED OPTICS

J. Opt. A: Pure Appl. Opt. **7** (2005) S438–S444 doi:10.1088/1464-4258/7/6/028

Multi-spectral laser detection and ranging for range profiling and surface characterization

A M Wallace[1], G S Buller[1], R C W Sung[1], R D Harkins[1], A McCarthy[1], S Hernandez-Marin[1], G J Gibson[1] and R Lamb[2]

[1] Heriot-Watt University, Riccarton, Edinburgh EH14 4AS, UK
[2] Qinetiq, St Andrews Road, Malvern, Worcestershire WR14 3PS, UK

Received 30 November 2004, accepted for publication 7 April 2005
Published 13 May 2005
Online at stacks.iop.org/JOptA/7/S438

Abstract
We describe a new multi-spectral system for range profiling and surface characterization based on time-correlated single photon counting (TCSPC). This system has six laser diode sources with discrete wavelengths in the range 630–972 nm arranged around the circumference of the aperture of a receiving Schmidt–Cassegrain telescope that focuses the multiple wavelength return onto an optical fibre. Single photon avalanche diodes are used to detect the six independent wavelength channels, separated by an optical routing module. We also describe two methods for detecting the numbers, positions, heights and shape parameters of signal returns in the spectra returned from several surfaces within the sensor field of view. The first method has two principal stages, non-parametric bump hunting and maximum likelihood estimation using Poisson statistics. Recently we have adopted a reversible jump Markov chain Monte Carlo approach that has the potential for better detecting hidden or closely overlapping returns.

Keywords: LaDAR, time-of-flight, photon counting, bump hunting, maximum likelihood estimation, Markov chain Monte Carlo

(Some figures in this article are in colour only in the electronic version)

1. Introduction

Laser detection and ranging (LaDAR) systems have been widely applied to distance measurement and 3D imaging in a wide range of applications including industrial metrology, environmental survey and remote target characterization [1]. Normally, LaDAR systems use a single wavelength, coherent source; however, if several laser sources at different wavelengths are used this allows us to combine distance measurement with an assessment of the surface colour signature, which augments the limited reflectance information that can be obtained by integrating a single laser wavelength return. We have adopted a particularly sensitive and accurate approach to LaDAR measurement based on time-of-flight, time-correlated single photon counting (TOF-TCSPC) [2, 3], capable of resolving returns from several discrete surfaces in the field of view of the sensor. In this paper, we describe the principles of the new multi-spectral sensor, and two different approaches for better interpreting the range information in a single wavelength return. As yet, each wavelength is processed independently, so the processing strategy is described with respect to a single wavelength distance measurement.

2. Optical system design and range measurement

In a TOF-TCSPC laser ranging system, typically a semiconductor laser is pulsed at a frequency of several megahertz with pulse duration of the order of tens of picoseconds. The laser beam is directed onto the measurement surface and the scattered returns are collected by an optical receiver and focused onto the detector, in our case a silicon single photon avalanche diode (SPAD). A typical single photon measurement may be subject to a jitter of 100–1000 ps, but several photon returns can be integrated and recorded as a histogram of number of received photons against delay time.

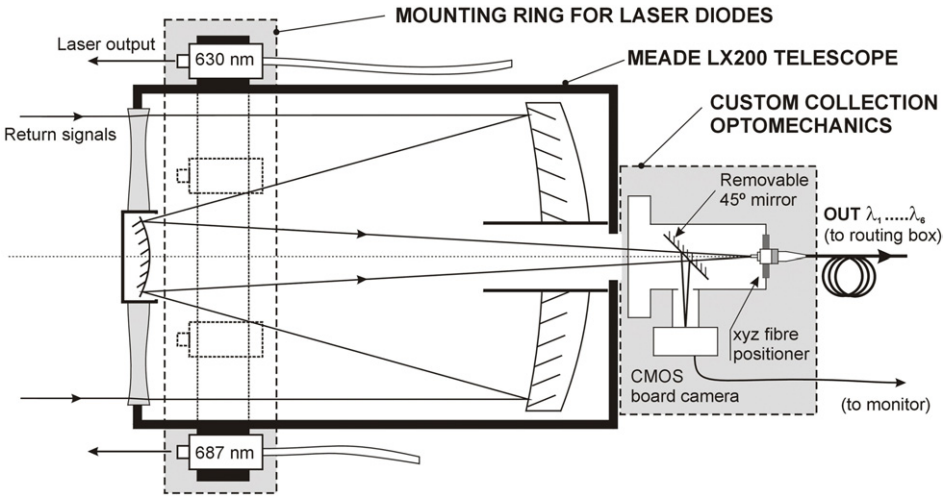

Figure 1. Schematic diagram of the adapted, receiving Meade Schmidt–Cassegrain telescope. The six laser diodes are equally spaced on a mounting ring surrounding the telescope aperture. The custom-built collection optomechanics included a removable 45° mirror and a XYZ fibre positioner to allow coarse and fine alignment of the return signal, respectively.

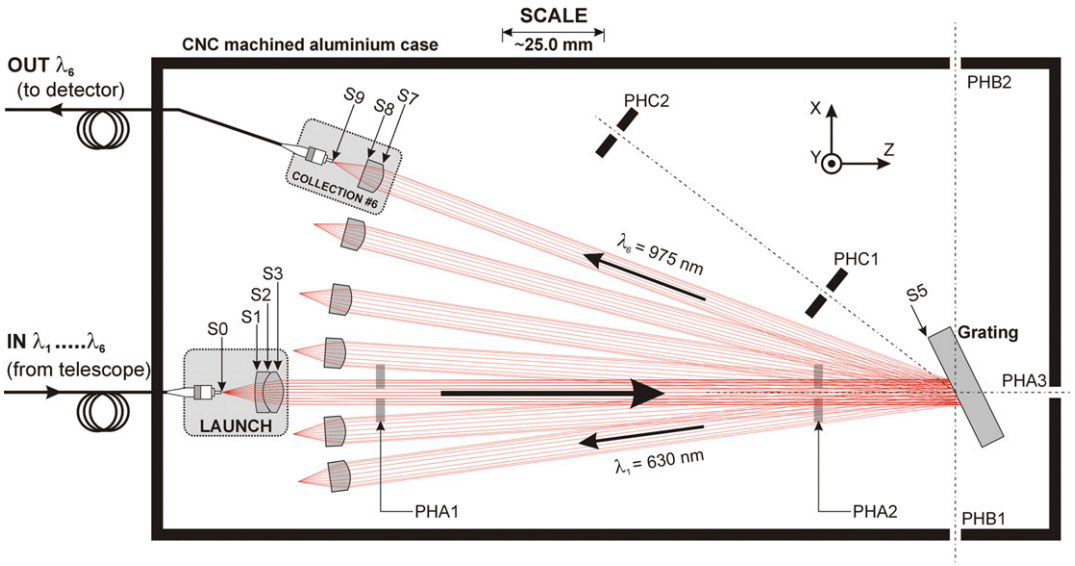

Figure 2. Schematic plan of the optical routing module. This shows the launch unit for the broadband signal received by the telescope, the diffraction grating that is used to separate the six discrete wavelengths and the replicated fibre-coupled lens assembly that focuses each signal onto each SPAD detector.

Processing these data can lead to a time resolution of less than 1 ps. The fundamentals of the approach are described fully in [2, 3].

Figures 1 and 2 illustrate respectively the transmitter/receiver assembly and the optical routing module that form the core of the optical design for the new multi-spectral sensor. This has six independent laser wavelengths, designed to act as a source for TOF-TCSPC distance measurements at ranges from a few hundred metres to several kilometres. In figure 1, the six transmitting laser diodes have wavelengths of 630, 687, 780, 842, 913 and 972 nm arranged in a ring around the outer of a 200 mm aperture, catadioptric Schmidt–Cassegrain telescope that focuses the multiple wavelength return onto an optical fibre mounted on a translation stage. Each laser mount has retaining springs and two 0.5 mm pitch thread screws that provide independent pitch and yaw adjustment and hence independent alignment of each laser onto the surface of interest. The CMOS camera is used for initial coarse alignment of the laser transmitters and receiver, and is removed from the optical path during the actual measurement of range. Fine alignment is achieved by the XYZ micropositioner that is adjusted to maximize the returned multiple wavelength signal.

The fibre from the telescope is connected to the input port of the custom-made optical routing module shown in figure 2. The launch unit consists of a 9 mm diameter, 12 mm effective focal length (EFL) achromat lens (surfaces S1–S3). This collimates the output from the fibre to a beam of nominal diameter 6 mm that is directed onto a plane-ruled reflectance grating approximately 200 mm away (labelled S5) that separates the six wavelengths in the horizontal plane.

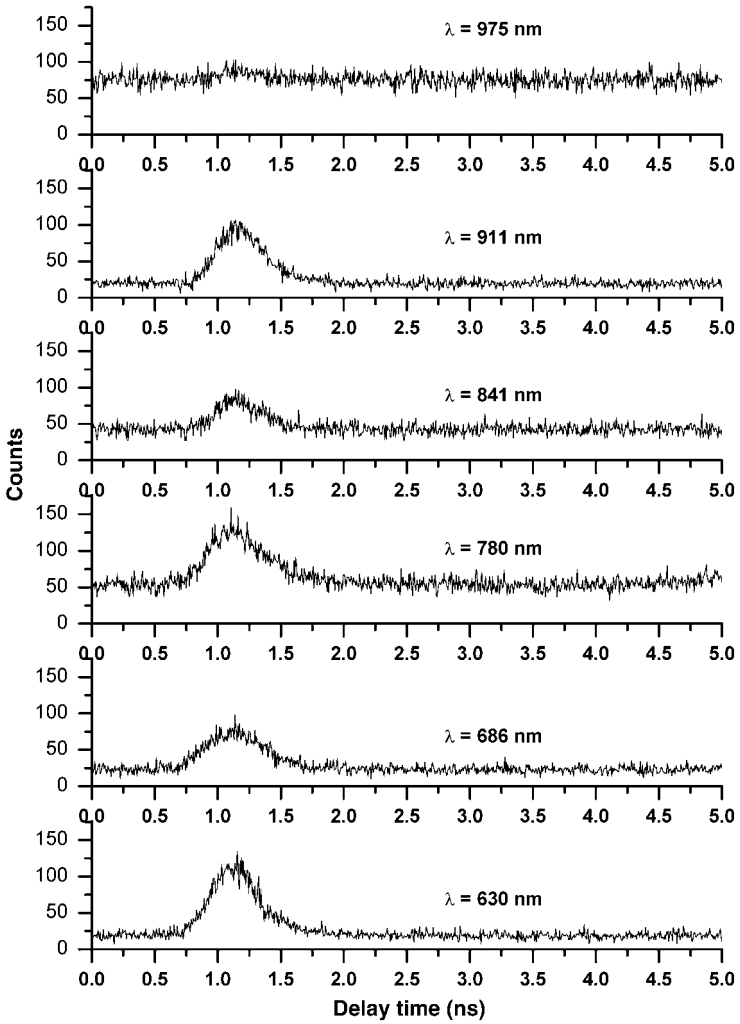

Figure 3. An example of the six wavelength responses from a corner cube at a distance of 2 km. The vertical axis shows the number of photon counts in each bin, the horizontal axis shows the delay time from a reference synchronization signal.

The grating has a ruled area of 26 mm × 26 mm with 1200 grooves mm^{-1}, a blaze wavelength of 760 nm and a blaze angle of 26.7°. The collection unit is based on a commercial FCPC fibre-coupler package. The lens, surfaces S7 (aspheric) and S8 (plano-type) in figure 2, has a diameter of 6.4 mm and an effective focal length of 11 mm at 633 nm. Since this corresponds to the lowest wavelength used in this system, a proprietary optical design software package was used to compute the image distances and spot sizes for each of the other, longer wavelengths. Multimode fibres of core sizes 50–100 μm diameter were selected for each particular channel on the basis of this optical modelling. The convenience and cost of using this particular fibre-coupled package outweighed the potential advantages in using lenses optimized for each spectral channel. The launch beam, grating and the individual collection modules for each channel were aligned with the aid of pinholes, labelled PH in figure 2, and an external He:Ne laser beam. When completed, the optical routing module had measured optical losses ranging from 2.7 dB at the 630 nm wavelength increasing to 10 dB at the 975 nm wavelength, consistent with the calculations of the optical design and analysis. The increase in wavelength results in increasing optical aberrations and associated defocus errors as lenses are operated further from their design wavelength, in addition to the spectral dependence of the grating loss.

In figure 3, we show an example of the six wavelength returns from a corner cube reflector at a range of 2 km. The temporal axis is shown with reference to the actual laser pulse transmitted to the target reflector—in this case delayed by approximately 8 μs—in order that aliasing does not play a part in these measurements. The large differences in background signal level are caused by a number of factors, including the optical throughput varying spectrally across the six channels due to differing diffraction efficiency, the spectral shape of the solar background and the differing choice of multimode fibre core diameter at the outputs of the optical routing module. We have observed, but not fully studied for this system, further problems in measurement due to beam scatter, scintillation and atmospheric loss. In general, beam scatter is caused primarily by atmospheric aerosols and results in a significant reduction in photon return count rate. Scintillation, caused by turbulence [4], causes fluctuations in the total count rate if, for example, measurements with short acquisition times are repeated. This can be observed as a twinkling appearance

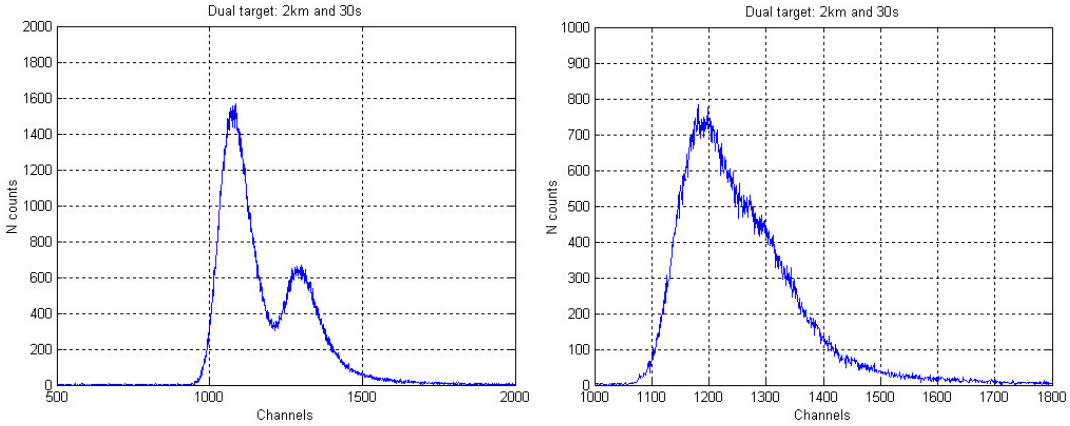

Figure 4. Reflections from two corner cubes separated by 20 cm (left) and 10 cm (right) at a distance of 2 km (630 nm).

of the return signal, particularly from a retro-reflector target. Atmospheric loss results simply in a reduction of the overall signal strength and is strongly dependent on the meteorological conditions.

3. Interpreting the photon count data

To interpret the data, we have used the parametric form of the expected temporal variation of the photon count distribution shown in equation (1). Although this piecewise exponential model is an operating model rather than a true model of the detector response, it is consistent with our own observations and those of Stellari *et al* [5] who investigated the behaviour of SPADs in some detail.

$$f(i,p) = \beta \begin{cases} e^{(-(i_1-i_0)^2/2\sigma^2)} e^{((i-i_1)/\tau_1)} & i \prec i_1 \\ e^{-(i_-i_0)^2/2\sigma^2} & i_1 \leqslant i \prec i_2 \\ e^{(-(i_2-i_0)^2/2\sigma^2)} e^{(-(i-i_2)/\tau_2)} & i_2 \leqslant i \prec i_3 \\ e^{(-(i_2-i_0)^2/2\sigma^2)} e^{(-(i_3-i_2)/\tau_2)} \times e^{(-(i-i_3)/\tau_3)} & i \geqslant i_3. \end{cases} \quad (1)$$

However, there are many cases of several returns that may be overlapping in position and possibly weak in comparison with the background level, either because they have been observed at a distance or because the reflectance in the direction of the sensor is low. Figure 4 shows an experiment in which two retro-reflecting corner cubes were placed 20 cm and 10 cm apart at a distance of 2 km from the sensor depicted in figure 1. In this example, the peaks are very well defined because the reflectors are nearly perfect; the problem is to detect the existence of the two peaks as the distance between them diminishes. On the other hand, figure 5 shows a photon count histogram that has many returns. In fact, this particular example is from the sensor described in [3] rather than that of figure 1, but the form of the data is exactly the same. However, this sensor allows us to operate in laboratory environment and is useful for experimental analysis of algorithms previous to field deployment. In this example, the multiple returns shown are due to several reflections from an alignment trace of a series of optical lens elements. Therefore, the observed photon

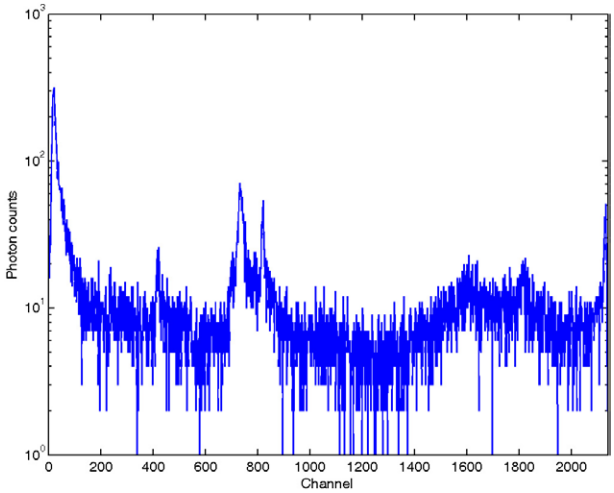

Figure 5. Multiple overlapping returns from a series of optical elements, taken under laboratory conditions, using a single spectral system described in [2].

histogram, $F(i, \Phi)$, is a statistical mixture constructed from a random sample of a distribution with density

$$F(i,\phi) = \sum_{j=1}^{n} f_j(i, p_j) + B \quad (2)$$

where Φ is the combined parameter vector, n is the number of terms in the summation, which depends on the number of surface returns. $f_j(i, p_j)$ denotes the functional form from the jth scatterer, where $f(\cdot)$ is defined by equation (1). The parameter B represents the background photon count level.

3.1. Non-parametric peak finding and maximum likelihood estimation

If the exact temporal response of the return from a single surface is known then this can be used to form a cross-correlation with the unknown signal data to maximize the peak-to-background level for each peak, provided the Poisson count distribution can be approximated by Gaussian distribution at high count levels [6]. However, there are several cases where

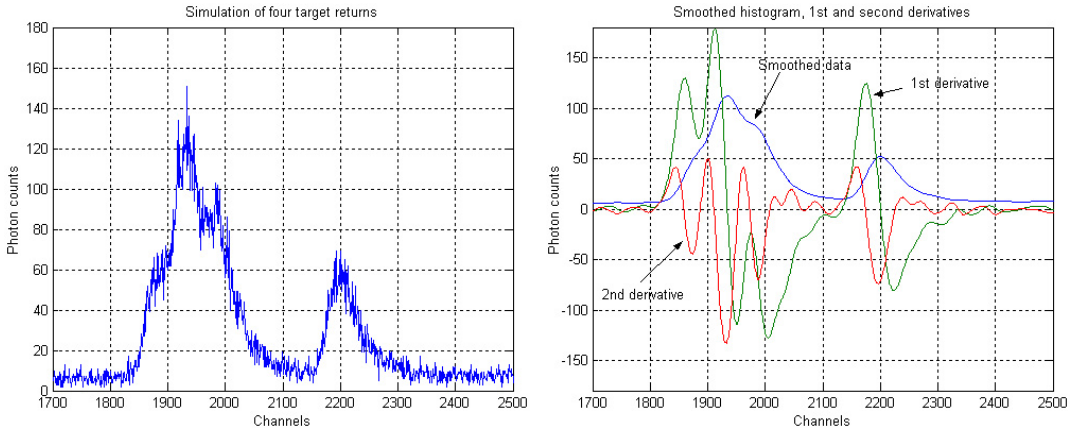

Figure 6. Application of kernel-based smoothing to obtain the first and second derivatives from multiple return, photon count data.

Table 1. Maximal likelihood estimation of the peak height, position and width/decay parameters using the representation of equation (1) and the simulation of figure 4. The true simulated peak heights and positions are shown in brackets. The computed background level was 5.92(5) counts. The estimates of the other parameters are shown for illustrative purposes and vary from the fitted reference as shown. (The reference parameters were taken from a real photon count return of a single, isolated peak, not shown).

Parameters	Reference	First peak	Second peak	Third peak	Fourth peak
β (counts)	540.03	95.61 (100)	69.65 (45)	38.91(50)	48.35(50)
σ (bins)	21.37	47.87	28.82	26.90	24.45
t_0 (bins)	2298.21	1937.79 (1935)	1984.86 (1990)	1879.32 (1884)	2201.19 (2200)
t_1 (bins)	2275.26	1884.54	1971.99	1862.88	2175.47
t_2 (bins)	2310.67	1944.02	2011.69	1889.97	2218.02
t_3 (bins)	2404.95	2067.23	2043.09	2011.59	2333.23
τ_1 (bins)	12.20	24.24	24.40	10.21	8.34
τ_2 (bins)	36.77	18.38	39.01	18.38	29.17
τ_3 (bins)	604.96	590.38	302.47	603.53	599.10

the exact form is unknown, the temporal response is changed by atmospheric transmission, or it is broadened by the reflection of a diverged beam with a surface that is distributed in depth across the beam diameter. To deal with these cases, we apply a non-parametric, bump hunting procedure [7] that provides an initial estimate of the number, amplitude and positions of the suspected returns. This uses Gaussian filters of progressively decreasing standard deviation. Chaudhuri and Marron [8] have shown that there is a similarity between the statistical procedure of applying kernel density estimates and scale space filtering in computer vision. In their work, they derived SiZer (significant zero crossings of derivatives) maps, in which a zero crossing in a smoothed derivative at a certain scale was indicative of a mode, or peak, of a given width. However, in our approach, second derivative filters are also applied to the original data, and we detect peaks in the second rather than zero crossings in the first derivative. This arises primarily from the desire to detect multiple returns when indicated only by multi-tangentiality, such as that shown in the rightmost figure 4.

Figure 6 shows an example of this process applied to a simulated photon count histogram having four closely separated returns. The use of simulated data allows comparison of the method against ground truth; the signal amplitudes are 50, 100, 45 and 50 counts at peak positions of 1884, 1935, 1990 and 2200 bins respectively, against a background of five counts. Concentrating on the second derivative data, there are negative peaks at 1935 and 2200 bins corresponding to the modes, but the co-tangential points at 1884 and 1990 bins are also highlighted. At 1884 bins, where the first derivative is *positive*, the existence of a further *negative* peak in the curvature shows a possible additional return. At 1990 bins, where the first derivative is *negative*, the existence of a further *positive* peak in the curvature shows an additional return.

Once the initial estimate is obtained, we compute a maximum likelihood estimate [9] (MLE) of the set of parameters $\phi = \{p_1 \cdots p_n, B\}$ that best explain the observed data. However, we wish to detect returns of low magnitude so that the Gaussian approximation may not be valid. Therefore, the number of photons, c_i, in bin i, is considered as a random sample from a Poisson distribution, with expected mean and variance $F(i, \phi)$ given by $P(c_i) = \mathrm{e}^{-F(i,\phi)} \frac{F(i,\phi)^{c_i}}{c_i!}$. As negative counts are not possible, and the product term is typically very small for any significant number of bins, it is more common to use the logarithm of the MLE. Omitting a term due to the summation of total counts, c, this means minimizing

$$-2 \ln L(c|\phi) = 2 \sum_{i=1}^{N} [F(i, \phi) - c_i \ln F(i, \phi)]. \qquad (3)$$

The results of the final MLE process are shown in table 1, in which there is good detection of the four returns and agreement with the simulated values. However, the process in still dependent on the curvature analysis, and may still not resolve even more closely overlapping returns, which has lead us to consider an alternative approach described in the next section.

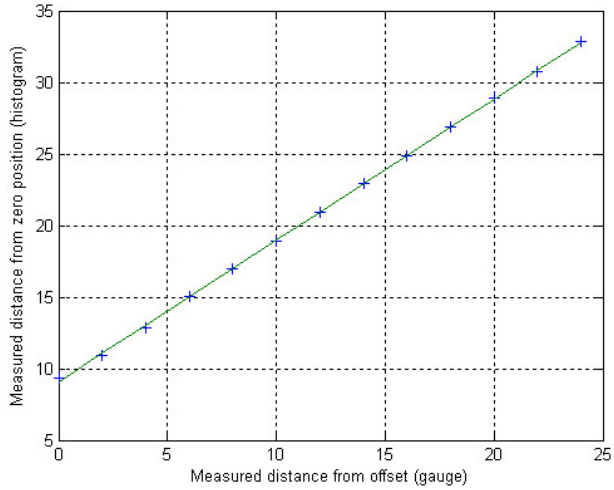

Figure 7. Graph showing the variation of measured separation between two corner cubes using the multi-spectral system at the 630 nm wavelength.

3.2. Reversible jump, Markov chain Monte Carlo

Markov chain Monte Carlo techniques [10] allow us to explore the full posterior distribution of the parameters of the mixture distribution of equation (2) from the data values, c, supplied by the photon count histogram. In effect, the parameters we seek are estimated from the values of a Markov chain whose limiting distribution is a target distribution π. In our case, π is the full posterior distribution, and a proposal distribution that governs the way in which the space of suitable parameters is explored. If we do not know how many returns are present, the number of parameters is not fixed since each new return adds new parameters.

The reversible jump Markov chain Monte Carlo (RJMCMC) [11] approach is an extension of the basic MCMC algorithm designed to allow jumps between different dimensional spaces. To make the problem less complex, we have assumed that the shape parameters of the return are known, i.e. that only β and t_0 vary in table 1 for example. As the background is also a variable this means that the final estimate has $(2n+1)$ parameters, i.e. two for each surface return and one for the background.

The different moves allowed are an update to the parameters of the returns in the mixture distribution, keeping n constant in equation (2), a random birth or death of a return, i.e. incrementing or decrementing n, and the random splitting of a peak into two peaks or merging of two peaks into a single peak. Assuming the current state of the parameter variable set is (n, ϕ), we propose a move to a state (n', ϕ'), drawn from the proposal probability density, $q_m(n', \phi', n, \phi)$. The full posterior distribution, $\pi(n, \phi|c)$, can be approximated by the product of the likelihood function that includes the current number of returns, n, i.e. $L(c|n, \phi)$, and the full prior distribution of the number of peaks and the set of parameters, $\pi(n, \phi)$, by means of Bayes theorem. The proposed move is accepted with a probability given by the following expression:

$$\alpha(n, \phi, n', \phi') = \min\left\{1, \frac{\pi(n', \phi'|c)}{\pi(n, \phi|c)} \frac{q_m(n', \phi', n, \phi)}{q_m(n, \phi, n', \phi')}\right\}. \quad (4)$$

If we do not change the number of returns, we have a conventional step for improving the current return parameters in a state space of fixed dimension. Equation (4) reduces to the Metropolis–Hastings acceptance probability,

$$\alpha(\phi, \phi') = \min\left\{1, \frac{\pi(\phi'|c)}{\pi(\phi|c)} \frac{q_1(\phi', \phi)}{q_1(\phi, \phi')}\right\}. \quad (5)$$

Whereas the target distribution is given by the shape parameters of the SPAD return, the proposal distribution is chosen to be representative of the solution space, yet to allow rapid convergence to a limiting solution. We have chosen gamma distributions to propose updates to the amplitude parameters, and a normal distribution for updates to the positional parameter, to allow a random walk in the parameter space. Updates are proposed independently to each parameter. Hence,

$$q_1(\phi, \phi') = \Gamma(1.5, B) \prod_{j=1}^{n} \Gamma(1.5, \beta_j) N(t_{0j}, \sigma^2). \quad (6)$$

A birth, death, split or merge implies a change in the parameter space (n varies). In this case the reversible jump is needed and the acceptance probability reduces to

$$\alpha(n, \phi, n', \phi') = \min\left\{1, \frac{\pi(n', \phi'|c)}{\pi(n, \phi|c)} \frac{r_m(\phi')}{r_m(\phi) q_2(u)} \left|\frac{\delta(\phi')}{\delta(\phi, u)}\right|\right\}. \quad (7)$$

Here, $r_m(\cdot)$ is the probability of choosing a move of type m when in state ϕ, and u is a vector of continuous random variables. This ensures the reversibility of the deterministic function $\phi' = h(\phi, u)$ and allows the move to a higher dimensional space. $q_2(\cdot)$ is the joint probability density function of u. The third, Jacobian term in equation (7) ensures the 'dimension-balancing' condition for reversible jumps.

For a birth we have to make a choice for the initial parameters of the proposed new peak. In practice we again use gamma (amplitude) and uniform (position) distributions. For a death, we choose a peak at random from the existing peaks. The split and merge moves are more complicated. Initially, a single peak is chosen at random for a split, but the positions and amplitudes of the new peaks are chosen in a more deterministic fashion that takes into account the need to equate the total mass of the two new peaks with the original single peak. For a merge, the two initial peaks must be within a temporal separation below a certain threshold and again, mass balancing is considered. Full details of the process are explained in [12].

4. Experimental results

In figure 4, we show two examples from a series of experiments to test the range resolution of the multi-spectral system using a pair of reflecting corner cubes at distances of 330 m and 2 km at collection times of 0.1, 1 and 10 s. As the histograms are relatively undemanding, these data have been processed by the MLE method. Figure 7 shows a graph of the distance measured against 'ground truth' provided by a ruled gauge to an accuracy of 1 mm. A regression fit to the line is $y = 9.09 + 0.99x$ (cm), with a mean absolute error of 0.6 mm between the laser and gauge measured data.

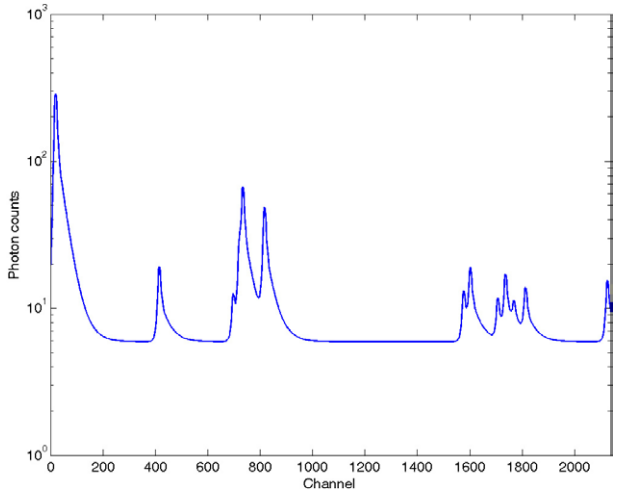

Figure 8. Application of the RJMCMC approach to detect and reconstruct the several returns from the optical system. The original histogram data are shown in figure 5.

In figure 8, we illustrate the ability of the RJMCMC approach to find multiple peaks in the data acquired from the optical assembly, for which the original photon count data are shown in figure 5. As the system was enclosed, we cannot compare the absolute positional parameters with ground truth, although we have done extensive simulations that do show good agreement between the simulated and the retrieved values. In this particular example of real data, thirteen peaks are found, many of which overlap.

5. Conclusions

In this paper we have presented work on the design of a multi-spectral LaDAR system using time-correlated single photon counting to determine the range and spectral signature of objects using several wavelengths. We have also presented analyses of the resultant data histograms using bump hunting, maximum likelihood and reversible jump Markov chain Monte Carlo techniques.

In experiments to resolve depth from reflecting surfaces at several kilometres, we have shown good agreement between the processed parameters and ground truth using maximum likelihood estimation. Further experiments using reversible jump Markov chain Monte Carlo algorithms have shown the potential to detect 'hidden' returns that may not be found by a bump hunting process. Future work is directed towards improving this technique, and to the incorporation of spectral or spatial constraints in a scanned image.

Acknowledgments

The authors would like to acknowledge the support of Qinetiq Ltd, BAE SYSTEMS and the Royal Society for different sections in this work.

References

[1] Amann M C, Bosch T, Lescure M, Myllyla R and Rioux M 2001 Laser ranging: a critical review of usual techniques for distance measurement *Opt. Eng.* **40** 10–9

[2] Wallace A M, Buller G S and Walker A C 2001 3D imaging and ranging by time-correlated single photon counting *IEE J. Comput. Control* **12** 157–68

[3] Massa J S, Buller G S, Walker A C, Smith G R, Cova S, Umasuthan M and Wallace A M 2002 Optical design and evaluation of a three-dimensional imaging and ranging system based on time-correlated single-photon counting *Appl. Opt.* **41** 1063–70

[4] Churoux P, Besson C and Bouzinac J P 2000 Model of a burst imaging lidar through the atmosphere *Laser Radar Technology and Applications* (*SPIE* vol 4035) (Bellingham, WA: SPIE Optical Engineering Press) pp 324–31

[5] Stellari F, Zappa F, Cova S, Porta C and Tsang J C 2001 High-speed CMOS circuit testing by 50 ps time-resolved luminescence measurements *IEEE Trans. Electron Devices* **48** 2830–4

[6] Umasuthan M, Wallace A M, Massa J S, Buller G S and Walker A C 1998 Processing time-correlated single photon data to acquire range images *IEE Proc. Vis. Image Signal Process.* **145** 237–43

[7] Harezlak J 1998 Bump hunting in regression data revisited *MPhil Thesis* Simon Fraser University, British Columbia

[8] Chaudhuri P and Marron J S 1999 SiZer for exploration of structure in curves *J. Am. Stat. Assoc.* **94** 807–23

[9] Hannam M D and Thompson W J 1999 Estimating small signals by using maximum likelihood and Poisson statistics *Nucl. Instrum. Methods Phys. Res.* A **431** 239–51

[10] Gilks W R, Richardson S and Spieghalter D J 1995 *Markov Chain Monte Carlo in Practice* (London: Chapman and Hall)

[11] Green P 1995 Reversible jump Markov chain Monte Carlo computation and Bayesian model determination *Biometrika* **82** 711–32

[12] Hernandez-Marin S, Wallace A M and Gibson G J May 2005 Markov chain Monte Carlo algorithms for 3D ranging and imaging *IAPR Conf. on Machine Vision Applications (Tsukuba, May 2005)*